

# Reasoning is a Modality

Zhiguang Liu, Yi Shang

University of Missouri - Columbia

lz7fd@missouri.edu, shangy@missouri.edu

## Abstract

The Abstraction and Reasoning Corpus (ARC) provides a compact laboratory for studying abstract reasoning, an ability central to human intelligence. Modern AI systems, including LLMs and ViTs, largely operate as sequence-of-behavior prediction machines: they match observable behaviors by modeling token statistics without a persistent, readable mental state. This creates a gap with human-like behavior: humans can explain an action by decoding internal state, while AI systems can produce fluent post-hoc rationalizations that are not grounded in such a state. We hypothesize that reasoning is a modality: reasoning should exist as a distinct channel separate from the low-level workspace on which rules are applied. To test this hypothesis, on solving ARC tasks as a visual reasoning problem, we designed a novel role-separated transformer block that splits global controller tokens from grid workspace tokens, enabling iterative rule execution. Trained and evaluated within the VARC vision-centric protocol, our method achieved 62.6% accuracy on ARC-1, surpassing average human performance (60.2%) and outperforming prior methods significantly. Qualitatively, our models exhibit more coherent rule-application structure than the dense ViT baseline, consistent with a shift away from plausible probability blobs toward controller-driven reasoning<sup>1</sup>.

## 1 Introduction

The Abstraction and Reasoning Corpus (ARC) [Chollet, 2019] is a compact laboratory for studying abstract reasoning, an ability central to human intelligence. We believe that there is a qualitative difference between LLM-based AI systems and human intelligence that is not reflected by quantitative performance scores, although the accuracy (60.4%) of the recent SOTA AI method VARC proposed by the MIT group [Hu *et al.*, 2025] is comparable with the average human accuracy (60.2%) [LeGris *et al.*, 2024]. In this paper, we analyze the qualitative difference, and based on biological and

cognitive evidence [Murray *et al.*, 2014; Zeraati *et al.*, 2023; Huntenburg *et al.*, 2018] we model human’s ability of justifying an action by *decoding* the corresponding internal mental states. In contrast, modern AI systems, including LLMs [Brown *et al.*, 2020] and dense ViTs [Dosovitskiy, 2020]), are *sequence-of-behavior prediction machines*: they generate behavior and explanations as statistically plausible continuations of an observable trace.

We hypothesize that reasoning is a modality: reasoning should exist as a distinct internal channel, a *global controller state*, that separates from the low-level workspace on which rules are applied. When solving ARC tasks as a visual reasoning problem, We implement this idea by designing a role-separated transformer block in our deep neural network model that includes (i) a compact set of globally connected *controller tokens* and (ii) a large set of *workspace tokens* representing grid states of ARC puzzles. The controller has global access, while the workspace is local, deliberately restricted to prevent it from becoming an unconstrained carrier of global state. This design creates an explicit bottleneck in the global state and a controlled interface through which the global state can control local execution. In experiments, we evaluated our models following the VARC protocol and observed both quantitative gains and qualitative shifts consistent with controller-driven rule application, as shown in Figure 1.

The main contributions of this paper include a new approach to formulating reasoning as a modality and a new reasoning model designed to solve ARC problems with a global controller state implemented as a transformer block that is separated from the low-level workspace. The new model outperformed existing SOTA methods on ARC problems,

## 2 Related Work

**Hierarchical and recurrent reasoning architectures.** A line of work toward more human-like reasoning is to introduce architectural hierarchy, often motivated by evidence that biological cognition exhibits multi-level organizations [Murray *et al.*, 2014; Zeraati *et al.*, 2023; Huntenburg *et al.*, 2018]. HRM [Wang *et al.*, 2025] and TRM [Jolicoeur-Martineau, 2025] are representative models: they incorporate hierarchical pathways and recurrence with the goal of separating higher-level state from lower-level processing. Although these models were designed as 2-channel hierarchical recurrent models, we think the designs do not by themselves en-

<sup>1</sup>Code base:[https://github.com/lz7fd/Reasoning\\_is\\_a\\_Modality](https://github.com/lz7fd/Reasoning_is_a_Modality)

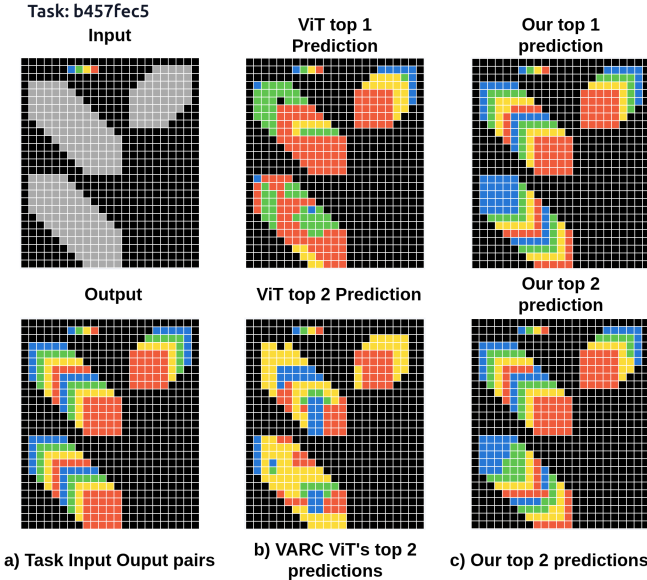


Figure 1: Solving an ARC puzzle by 2 types of reasoning: amortized fitting and controller-driven reasoning. Column (a) is the ARC puzzle input-output pairs. Column (b) has two predictions by the ViT based VARC. Column (c) contains two predictions by our new model. This example shows ViT predicts the output as plausible probability blobs, whereas our model has more structured rule application. See Figure 6 for corresponding layer-wise attention maps.

force role separation: if the workspace stream retains high-bandwidth global mixing, the intended controller/workspace distinction is not identifiable and can collapse into a single reasoning substrate.

**Vision-centric ARC solvers.** VARC [Hu *et al.*, 2025] demonstrates that ARC can be formulated as a unified vision-conditioned discrete image-to-image translation problem, combined with a 2-stage training paradigm. We adopt the VARC protocol for training, adaptation, and evaluation, and make one architectural change to their ViT [Dosovitskiy, 2020] backbone: we replace the dense ViT backbone with a role-separated transformer block that partitions global controller tokens from local workspace tokens via a structured attention pass. This isolates the contribution of architectural role separation while keeping the overall training and evaluation pipeline aligned with established ARC practice.

### 3 Failure of AI Systems in Human Simulation

Many of today’s AI systems are fundamentally *sequence-of-behavior prediction machines*: they map an observed behavior history to the next behavioral token (or the next segment of a behavioral trace). Examples include large language models (LLMs), which predict the next text token, and vision transformers (ViTs), which predict task-relevant token sequences. Although these systems can achieve remarkable performance, their *reasoning mechanisms* differ qualitatively from humans’.

In this section, we present a task inspired by a core component of human intelligence: humans can often *explain*

their own behavior by decoding an internal mental state that causally produced the behavior. Supported by biological and cognitive evidences that human brain works in hierarchical data processing and temporal separation [Murray *et al.*, 2014; Zeraati *et al.*, 2023; Huntenburg *et al.*, 2018], we think that pure behavior-sequence predictors may fail in this setting due to a missing structural component – a readable, causally relevant mental state.

#### 3.1 The Smile Explanation Task

**Setup.** Assume a human  $H$  and a sequence-of-behavior prediction agent  $S$ . We grant  $S$  maximal behavioral competence: conditioned on an observed behavior history,  $S$  can match the next human behavior token. The goal of this example is not to dispute behavioral imitation, but to isolate a mechanistic gap between *acting* and *explaining*.

Let time be discrete  $t \in \{t_0, \dots, t_n\}$ . Let  $x_t$  denote external input and  $b_t$  denote an observable behavior token (e.g., facial expression), where  $b_t \in \{\text{none}, \text{smile}\}$ . Consider an interval with no external input

$$x_{t_0:t_n} = \emptyset,$$

and an observable behavior sequence for both systems:

$$b_{t_0:t_{n-1}} = \text{none}, \quad b_{t_n} = \text{smile}.$$

Thus,  $H$  and  $S$  are indistinguishable from their behaviors over  $t_0, \dots, t_n$ .

**Human mechanism (state decoding).** We model the human as maintaining an internal mental state  $m_t \in \mathbb{R}^d$  that is not directly observable. Behavior is a readout of this state,

$$b_t^H = D_{\text{face}}(m_t), \quad (1)$$

and, when queried at  $t_n$  with  $q = \text{“Why are you smiling?”}$ , the human produces an explanation by decoding the state into language:

$$y^H = D_H(m_{t_n}, q). \quad (2)$$

Importantly, words such as “funny” are linguistic descriptions produced by  $D_H$ .

**Behavior-sequence mechanism (post-hoc explanation).** The agent  $S$  is defined as a conditional behavior predictor: it selects the next behavior token based on the observed behavior history:

$$b_{t_n}^S = \arg \max_b p_\theta(b \mid b_{t_0:t_{n-1}}^S), \quad (3)$$

where  $\theta$  is model parameter. When asked “Why are you smiling?” at time  $t_n$ ,  $S$  generates an explanation conditioned on the observable history:

$$y^S = D_S(b_{t_0:t_n}^S, q). \quad (4)$$

**Mechanistic gap and hallucination.** For the human, both the action and the explanation are decodes of a shared internal state. By contrast, the behavior-sequence predictor generates the smile behavior by likelihood maximization (3) and generates an explanation from the observable trace (4). We refer to this mechanism of post-hoc rationalization without subjective experience as “hallucination” in the context of this paper.

The smile explanation task separates two mechanisms: *state-decoding intelligence* (human modeling) vs. *behavior-sequence intelligence* (behavior-driven). Mitigating this form of agent hallucination requires a structural change to the agent: introducing an explicit, readable controller state that drives both behavior and explanation.

### 3.2 Reasoning Is a Modality

Some recent “reasoning models” [Agarwal *et al.*, 2025; Guo *et al.*, 2025] introduce an explicit intermediate *thinking* trace, often as additional tokens, before emitting a final answer. We viewed this approach as simulating a mental state channel: the model first constructs an intermediate representation that plays the role of a *simulated mental state*, then decodes the final answer from that state.

Let  $\hat{z}$  denote a “thinking” sequence. A reasoning model produces

$$\hat{z} \sim p_\theta(z \mid \text{input}), \quad \hat{y} \sim p_\theta(y \mid \text{input}, \hat{z}).$$

where  $z$  is a thinking state and  $y$  is an output.

Empirical results of reasoning models showed performance improvement when decoded from a thinking state instead of straight post-hoc rationalization.

The success of “reasoning models” suggests that constructing and decoding explicit intermediate states can improve performance, which motivates our hypothesis:

**Reasoning Is a Modality Hypothesis.** Reasoning should exist as a distinct internal channel, a *global controller state*, that is separate from the low-level workspace on which rules are applied.

In the remainder of the paper, we operationalize this hypothesis by designing a role-separated transformer block to solve ARC puzzles.

## 4 ARC as a Visual Reasoning Problem

VARC [Hu *et al.*, 2025] demonstrates that ARC can be formulated as a vision-conditioned, discrete image-to-image translation problem under a unified training and evaluation protocol. We adopt VARC’s visual modeling, data augmentation, and test-time training (TTT) pipeline, and focus on a key architectural change: replacing the dense ViT backbone with a role-separated transformer that explicitly partitions tokens into a small set of controller tokens as high-level global controller state and a large set of workspace tokens as low-level workspace. Unlike HRM interprets human brain separation of 4–8 Hz slow theta waves and 30–100 Hz fast gamma waves as slow and fast neurons [Başar *et al.*, 2001; Buzsáki, 2006; Pahor and Jaušovec, 2014; Tort *et al.*, 2009], we design 2 synchronized channels with low and high bandwidth reflected by the number of tokens.

### 4.1 Problem Formulation

An ARC task  $T$  contains an unknown transformation that maps an input grid  $x$  to an output grid  $y$ . Each grid is a 2D array of categorical values (colors). Specifically, for a fixed number of colors  $C$  and a maximum spatial size  $H \times W$  (with  $H, W \leq 30$ ),

$$x \in \{0, \dots, C-1\}^{H \times W}, \quad y \in \{0, \dots, C-1\}^{H \times W}.$$

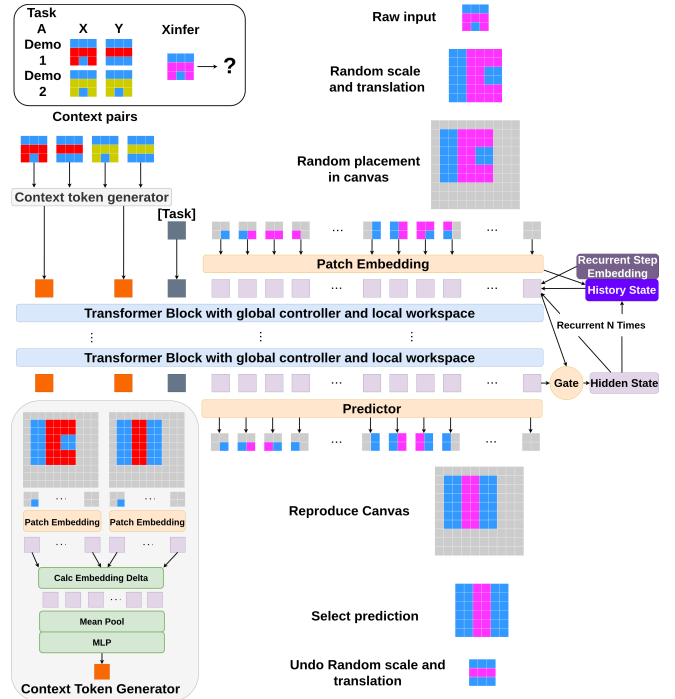


Figure 2: Workflow of our new reasoning model. We adopt the VARC method for input transform, visual embedding, and output projection. Details of our new transformer block are shown in Figure 3. The transformer blocks can be stacked up.

The task provides a small demonstration set of input-output pairs

$$D_{\text{demo}}^T = \{(x_i, y_i)\}_{i=1}^m,$$

where typically  $m \in \{2, 3, 4\}$ , and an inference set

$$D_{\text{infer}}^T = \{x_j\}_{j=1}^n,$$

where  $n \in \{1, 2\}$ . At test time, the model is given  $D_{\text{demo}}^T$  and a query input  $x_{\text{infer}}$  from  $D_{\text{infer}}^T$ , and is asked to predict  $y_{\text{infer}}$ .

In the VARC method, offline training learns shared parameters across tasks using demonstration sets of all available tasks, while task-specific adaptation is performed at test time via test-time training (TTT) using the demonstration set of the target task. Our method follows the same protocol.

### 4.2 A New Reasoning Model

Figure 2 shows our new reasoning model. Following the VARC method, each grid of an ARC puzzle is first embedded into a larger canvas (e.g.,  $64 \times 64$ ) using a family of stochastic, task-preserving augmentations (e.g., rotations, translations, and scale changes), with a fixed border to avoid boundary artifacts. Let  $\tilde{x}$  denote the augmented canvas representation of the input grid.

We then tokenize  $\tilde{x}$  using non-overlapping  $p \times p$  patches ( $p = 2$  in our experiments). Each patch is embedded into a  $D$ -dimensional vector via a linear patch embedding, and a 2D positional embedding is added. This yields the workspace token sequence

$$w = [w_1, \dots, w_L] \in \mathbb{R}^{L \times D},$$

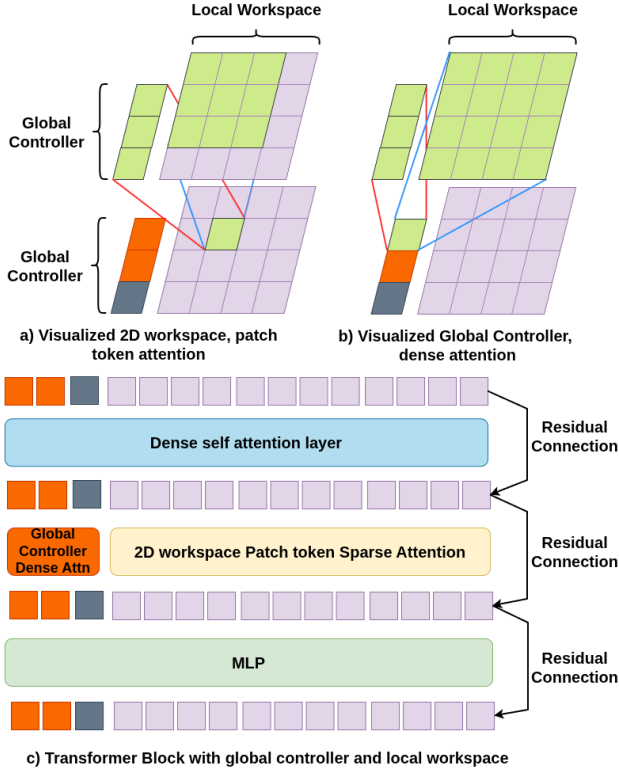


Figure 3: The internal structure of the new role-splitting transformer block. (a) and (b) show the attention mechanism of the patch token and controller token, and (c) shows the block structure.

where  $L$  is the number of patches on the canvas.

Unlike dense ViTs, which treat all tokens symmetrically, our model also constructs a small set of controller tokens from the task demonstrations  $D_{\text{demo}}^T$  (described below). The controller tokens and workspace tokens are concatenated to form the initial hidden state sequence:

$$h^{(0)} = [g; w] \in \mathbb{R}^{S \times D},$$

where  $g$  denotes controller tokens and  $S$  is the total token length.

As shown in Figure 2 and 3, our design imposes an explicit role separation: (i) a small controller intended to carry and process global states and (ii) a large workspace intended to carry and process grid states. The controller is given global access, while the workspace is deliberately constrained to limit global mixing.

### Global Controller

The global controller consists of a task token and a set of context tokens derived from ARC task demonstrations. The task token is a learned embedding. During offline training, each training task is associated with an identifier and thus a learnable task embedding; at test time, a new task token will be adapted during TTT.

The context tokens are computed from demonstration pairs as shown in Figure 2. For each demonstration  $(x_i, y_i) \in D_{\text{demo}}^T$ , we apply the *same* augmentation family used for the query grid so that the representation is consistent under the

VARC protocol. We embed the augmented inputs into patch tokens using the same patch embedding and positional embedding, producing token sequences  $E(\tilde{x}_i), E(\tilde{y}_i) \in \mathbb{R}^{L \times D}$ . We then computer token-level difference

$$\Delta_i = E(\tilde{y}_i) - E(\tilde{x}_i),$$

across spatial tokens and project with a small MLP to obtain a single context token  $c_i \in \mathbb{R}^D$ . Repeating this for  $m$  demonstrations yields  $m$  context tokens.

Finally, the controller token sequence is

$$g = [\tau_T, c_1, \dots, c_m] \in \mathbb{R}^{P \times D},$$

where  $\tau_T$  is the task token and  $P = m + 1$ .

The full token sequence is then formed by concatenating  $g$  with workspace tokens  $w$ :

$$h^{(0)} = [g; w].$$

After initialization,  $h^{(0)}$  is processed by our role-separated transformer blocks (Figure 3c). Each block contains two self-attention passes and an MLP: (i) a standard dense attention pass (as in ViT) and (ii) a structured attention pass that enforces the controller–workspace separation. In the structured pass, controller tokens can attend to all tokens (Figure 3b), while workspace tokens are restricted to attend only to controller tokens and a small local neighborhood on the workspace (self and 8 neighbors in a  $3 \times 3$  patch neighborhood, as shown in Figure 3a). This restriction is designed to preserve local grid consistency while preventing workspace tokens from becoming a full-capacity carrier of global task states.

### Local workspace

The local workspace tokens are the patch embeddings of the augmented query grid. In a dense ViT, workspace tokens can attend to all other workspace tokens, which makes them capable of representing both global task structure and local pixel state. In contrast, our structured pass intentionally limits workspace attention to reduce global information mixing: each workspace token can consult the controller (global task state) and a small local neighborhood (for local consistency and corrections), but it cannot aggregate information from the full grid.

Specifically, under dense attention, a workspace token may attend to  $S$  tokens (controller + all workspace tokens). However, under our structured pass, a workspace token attends to at most

$$P + 1 + 8 \leq 14$$

tokens (controller tokens + self + 8 neighbors, as shown in Figure 3a), which is orders of magnitude smaller than dense global attention on a  $64 \times 64$  canvas with  $2 \times 2$  patches. This bottleneck makes the controller a natural locus for global task information while leaving the workspace primarily responsible for representing and updating the grid state.

### 4.3 Recurrent Controller

Prior work [Jolicoeur-Martineau, 2025] [Wang *et al.*, 2025] suggests that increasing effective depth via recurrence can improve performance on ARC-like reasoning tasks under

fixed parameter budgets. We therefore apply a lightweight recurrent wrapper around the transformer [Vaswani *et al.*, 2017] stack to increase effective depth without increasing the number of parameters. Let  $f_\theta(\cdot)$  denote the encoder (the stack of role-separated transformer blocks). For  $K$  recurrent steps, we maintain a current state  $h^{(k)}$  and a history state  $s^{(k)}$  (an exponential moving average). At step  $k$ , we compute an update by applying the encoder and a simple gate:

$$u^{(k)} = f_\theta\left(h^{(k)} + s^{(k)}\right), \quad \gamma^{(k)} = \sigma\left(W[h^{(k)}; s^{(k)}]\right),$$

and apply a gated residual update

$$h^{(k+1)} = h^{(k)} + \gamma^{(k)} \odot u^{(k)}.$$

The history is updated with EMA coefficient  $\alpha$ :

$$s^{(k+1)} = \alpha s^{(k)} + (1 - \alpha) h^{(k+1)}.$$

This recurrence is not intended to emulate an RNN over time; rather, it provides iterative refinement over a fixed input, consistent with the view that controller-driven reasoning can be implemented as repeated rule execution over a workspace.

#### 4.4 Output projection

After the final recurrent step, a linear prediction head maps each workspace token back to categorical logits for the corresponding  $p \times p$  patch. The patch-level logits are then reshaped and assembled into a full-grid prediction on the augmented canvas. Finally, we invert the augmentation (undoing translation/rotation/scale and crop the border) to obtain logits over the original  $H \times W$  grid, and decode the predicted output grid  $y$  by arg max over colors at each cell, as shown in Figure 2.

### 5 Ablation study and Experiments

#### 5.1 Two-Stage training and inference

We follow VARC’s two-stage paradigm: (i) offline training shared across tasks and (ii) test-time training (TTT) [Akyürek *et al.*, 2024; Sun *et al.*, 2020] for per-task adaptation, followed by (iii) inference with multi-view augmentation. Specifically, a single network  $f_\theta$  is trained jointly over all training tasks  $T_{\text{train}}$  (e.g., 400 tasks in ARC-1) using only their demonstration sets  $D_{\text{demo}}^T$ . Following VARC, we expand each training task with RE-ARC [Hodel, 2024] by 1000 demos during offline training (which is the same protocol as VARC by default). The inference sets  $D_{\text{infer}}^T$  of training tasks are withheld and used only for validation, aligned with the VARC protocol.

At test time, for each task  $T \in T_{\text{test}}$ , we perform task-specific adaptation via TTT using the provided demonstrations  $D_{\text{demo}}^T$ . A task token is initialized for the new task and optimized during TTT. The adapted model then predicts  $y_{\text{infer}}$  from the query input  $x_{\text{infer}}$ , defining a task-conditioned mapping:

$$F(x_{\text{infer}} \mid D_{\text{demo}}^T) \mapsto y_{\text{infer}}.$$

Inference is performed under augmented views of  $x_{\text{infer}}$  as in VARC. The predictions across views are consolidated by majority voting, and we retain the two most frequent outputs to match the ARC pass@2 protocol. A task is counted as solved if either of the two retained predictions matches the ground-truth output.

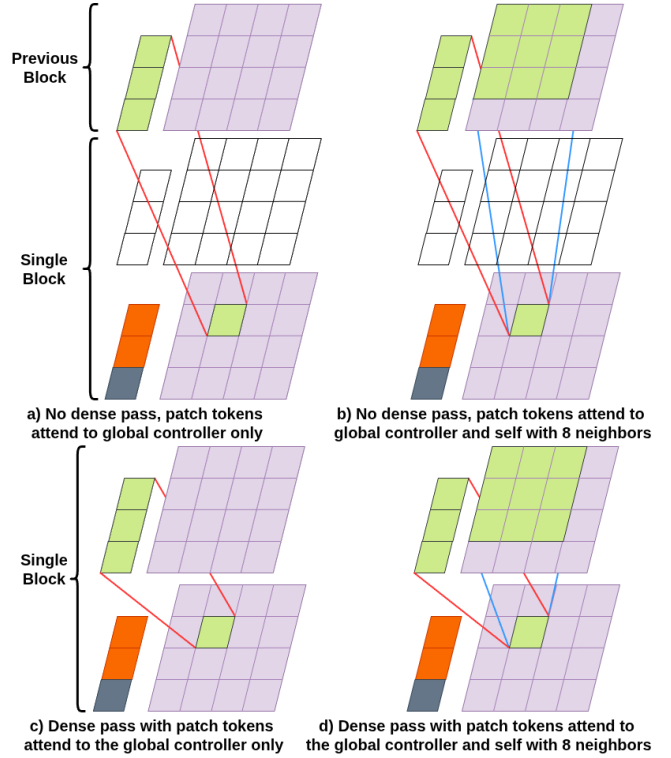


Figure 4: Four architecture variants of our new transformer block for separating global controller from local workspace.

#### 5.2 Architecture Variants of Transformer Block

As part of the ablation study, we train multiple model variants under controlled settings. Unless otherwise stated, all models use the same base configuration adopted from VARC: embedding dimension 512, encoder depth 10, canvas size  $64 \times 64$ , and  $2 \times 2$  patching.

Our core design hypothesis is that abstract reasoning benefits from an explicit role separation between a compact *global controller* (reasoning modality) and a large *local workspace* (grid state). Within a transformer block, there are multiple ways to impose such a separation. Figure 4 shows four candidate architectures:

- Architecture a: No dense self-attention; controller attends globally; workspace attends only to controller.
- Architecture b: No dense self-attention; controller attends globally; workspace attends to controller and a local neighborhood (self + 8 neighbors).
- Architecture c: Dense self-attention followed by a structured pass; in the structured pass, controller attends globally; workspace attends only to controller.
- Architecture d: Dense self-attention followed by a structured pass; in the structured pass, controller attends globally; workspace attends to controller and a local neighborhood (self + 8 neighbors).

For compact notation, we denote an architecture by  $\text{arch-}r$ , where  $\text{arch} \in \{a, b, c, d\}$  and  $r$  is the number of

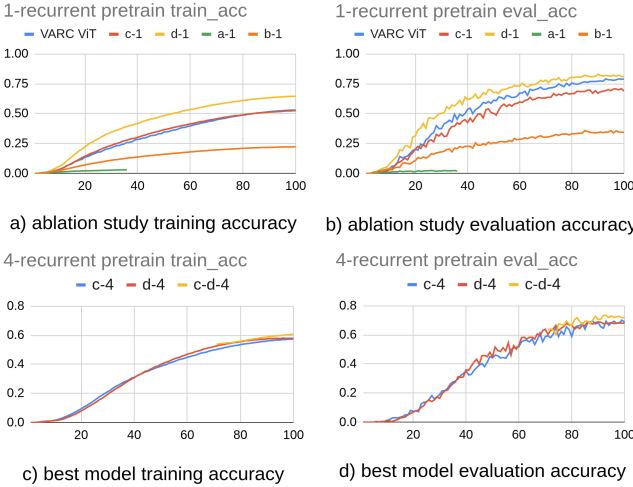


Figure 5: Ablation study and best models: training and evaluation accuracy curves across 100 training epochs for selected architectures of our new transformer block in pretraining. (a) and (b) compare the results of 5 basic architectures; while (c) and (d) show the results of 3 best models.

recurrent unroll steps (effective depth = base depth  $\times r$ ). For example, d-1 denotes architecture d with  $r = 1$ .

Our offline training objective is the sum of the output-grid cross-entropy [Long *et al.*, 2015] and an optional mid-loss used for deep supervision [Lee *et al.*, 2015] under recurrence. Specifically, for recurrent models, we optionally project an intermediate hidden state to logits and apply a cross-entropy loss. In our implementation, models with  $r \in \{1, 2\}$  are trained without mid-loss for stability and simplicity, while deeper recurrent settings use mid-loss.

We train these architectural variants under identical data and optimization settings to isolate the effect of role separation. Figure 5 shows training and evaluation curves of several representative architectures. Architecture a and b performed poorly on ARC tasks due to lack of dense self attention. Architecture c was comparable with the ViT baseline in training accuracy, but exhibits a smaller train-eval disparity under RE-ARC augmentation, suggesting a shift away from superficial distribution matching toward more rule-consistent generalization. Architecture d obtained the best training and evaluation accuracy.

For  $r = 4$ , we observed that training architecture d end-to-end did not always outperform architecture c, as shown in Figure 5 (c) and (d). Empirically, the best variant was obtained by *staged* training: we first trained architecture c 100 epochs and then enabled the structured neighborhood as in architecture d in the next 30 epochs, yielding the variant c-d-4, our best model.

### 5.3 Test-Time Training

We follow VARC’s test-time training (TTT) paradigm: for each unseen task  $T$ , we adapt the pretrained model using only this task’s demonstration set  $D_{\text{demo}}^T$ . Each TTT epoch samples stochastic, task-preserving augmentations of the demonstrations, including rotation/translation/scale and resolution

augmentation as in VARC, and optimizes a supervised loss on the augmented targets. Unless otherwise stated, TTT updates the model end-to-end, including the task token. We reset the optimizer state at the start of each task adaptation run.

We evaluate three TTT strategies, chosen to isolate (i) optimization budget and (ii) the effect of auxiliary objectives that encourage exact-match correction under ARC’s strict evaluation.

**TTT1 (VARC baseline).** We run 100 epochs of TTT using the default VARC step size and schedule, and optimize only the standard grid cross-entropy. This setting matches the original VARC protocol and serves as our baseline.

**TTT2 (same compute, smaller step size).** We reduce the learning rate by  $3 \times$  and increase the TTT budget by  $3 \times$  (300 epochs). This keeps the overall optimization budget comparable to TTT1 while improving stability for deeper/structured backbones. We additionally allow early termination once the task reaches 100% training accuracy in a 3-epoch streak to avoid over-updating after convergence.

**TTT3 (TTT2 + auxiliary objectives).** TTT3 augments TTT2 with auxiliary losses designed for matching ARC evaluation exactly. The key components are: (i) *grid-level correctness supervision* via a lightweight correctness head computed from global patch features and (ii) *pixel-level error emphasis* that separates correct and wrong-pixel contributions so that sparse local errors remain visible to the optimizer even when the majority of pixels are already correct, which is similar to focal loss [Lin *et al.*, 2017]. In addition, we apply a small *reward shaping* rule: when a predicted grid is exactly correct, we down-weight the output cross-entropy and disable mid-loss supervision to prevent latent drift after the correct solution is reached.

**Inference Protocol.** Following the VARC protocol, a total of 510 augmented views of  $x_{\text{infer}}$  are consolidated by majority voting, and the two most frequent candidate grids (pass@2) are the output. A task is counted as solved if either candidate matches the ground truth. Reported results are pass@2 averaged across 4 seeds for 4 random trials.

### 5.4 Experimental Results

In our experiments, all models were trained from scratch using the VARC protocol, i.e. the same offline training pipeline (including RE-ARC augmentation) and the same inference-time multi-view voting in evaluation. For ARC-2, we did not use ARC-2 training tasks in offline pretraining; thus performance improvement on ARC-2 reflects out-of-distribution generalization and the effectiveness of test-time adaptation.

Table 1 compares the size and test accuracy of several VARC-ViT models and our proposed models with different recurrent depth and test time training strategies. The best single-pass model at  $r = 1$  is architecture d: dense attention followed by a structured pass where workspace tokens attend to the controller and a small local neighborhood. This result supports our design principle: reasoning signals should be mediated by controller tokens, while local consistency and corrections should remain available within the workspace through limited neighborhood access.

Table 1: Size and test accuracy comparison of several architectures of VARC-ViT and our proposed models with different recurrent depth and test-time-training strategies on ARC-1 and ARC-2.

Model	#param	Accuracy ARC-1	Accuracy ARC-2
VARC-ViT	18M	54.5	8.3
VARC-ViT-large	66M	53.0	-
d-1-TTT1	28M	56.6	6.9
d-1-TTT2	28M	56.4	7.71
d-1-TTT3	28M	55.5	8.3
c-2-TTT2	28M	58.0	8.3
c-d-4-TTT3	28M	<b>58.8</b>	<b>11.0</b>

Table 2: Performance comparison of our model c-d-4-TTT3 with previous methods (HRM, TRM, and VARC) on ARC-1 and ARC-2.

Method	#param	Accu. ARC-1	Accu. ARC-2
HRM	27M	40.3	5.0
TRM	7M	44.6	7.8
VARC-ViT	18M	54.5	8.3
VARC-ViT-large	66M	53.0	-
VARC-ViT-Unet-ensem	73M	60.4	11.1
c-d-4-TTT3	28M	<b>58.8</b>	<b>11.0</b>
c-d-4-TTT3-Unet-ensem	83M	<b>62.6</b>	<b>13.5</b>
Average human	-	60.2	-
Best human	-	98.0	100.0

For deeper recurrent unrolling ( $r = 4$ ), the best model (c-d-4) was obtained by 2-stage training: we first trained with architecture c (controller-only structured pass), then enabled local neighborhood attention in the structured pass during continued training. This procedure preserves the controller/workspace bottleneck while introducing local repair capacity after the backbone has already formed a stable global coordination regime. Model c-d-4-TTT3 achieved the best performance, outperforming VARC significantly on both ARC-1 and ARC-2.

Table 2 shows performance comparison of our model c-d-4-TTT3 with previous methods on ARC-1 and ARC-2. Our c-d-4 model with TTT3 training achieved  $58.8 \pm 0.7$  on ARC-1 and  $11.0 \pm 1.0$  on ARC-2 over 4 random trials. On average, it outperformed VARC-ViT by 4.3 on ARC-1 and 2.7 on ARC-2. When using the VARC-Unet [Ronneberger *et al.*, 2015] ensemble technique, c-d-4 model achieved **62.6%** on ARC-1 and **13.5%** on ARC-2, outperforming the reported VARC-ViT-Unet ensemble results significantly. It also performed better than the average human, which was reported by [LeGris *et al.*, 2024]. The best human was reported by [Foundation, 2026].

Figure 6 shows a visualization of layer-wise attention maps of our model d-1-TTT1 against those of VARC-ViT on an ARC puzzle example. Both models were trained and evaluated under the same condition. The ViT’s attention field

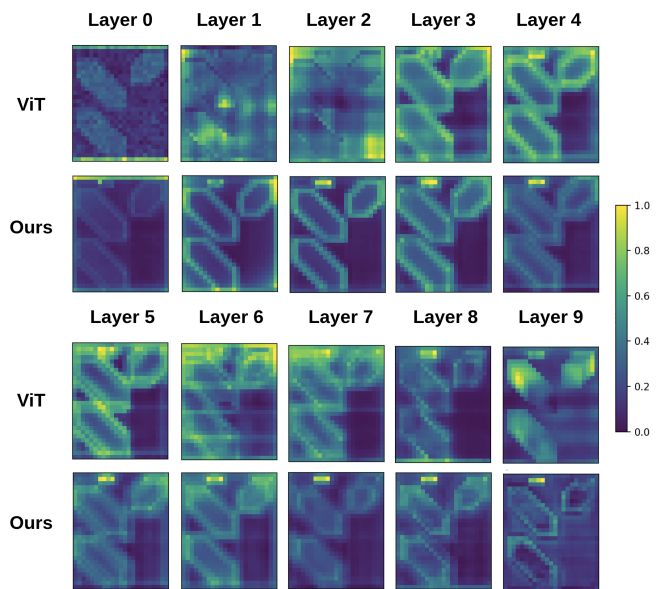


Figure 6: Visualization of layer-wise attention maps of our model d-1-TTT1 and VARC-ViT on an ARC puzzle example. Both models were trained and evaluated under the same condition. For the task, we performed ratio 2 up-scaling to the input grid. Each pixel would occupy exactly 1 patch so that the patch level attention was transformed into pixel level attention for better visualization.

progressively diffuses, shifting mixtures over the workspace, consistent with unconstrained global token mixing. In contrast, our model exhibits a stable, structured attention field that preserves coherent spatial primitives across depth, showing the effect that a global controller guides local workspace updates rather than allowing the workspace to become a full-capacity global carrier. At layer 1 and layer 2, ViT’s attention map is highly mosaic and fuzzy, which reflects the patch tokens are acting as the carrier of both high and low level information. From layer 3, the ViT attention maps start to show patterns similar to our model, although not as crisp.

## 6 Summary

In this paper, from the hypothesis that reasoning is a modality, we designed novel reasoning models to solve the challenging ARC puzzles as a visual reasoning problem. The key reasoning component of our models is a role-separated transformer block that splits global controller tokens from grid workspace tokens, enabling iterative rule execution. In experiments, our best model achieved outstanding performance on ARC-1 and ARC-2 test cases, reaching accuracy 58.8% on ARC-1 and 11.1% on ARC-2, outperforming the state-of-the-art VARC-ViT (54.5% and 8.3%, respectively). When ensembled with UNet, our model achieved 62.6% accuracy on ARC-1, surpassing both average human (60.2%) and VARC-ViT (60.4%). Qualitatively, this work suggests that lack of a grounded global state for decoding might be the qualitative deficiency of AI systems in human simulation. Our new reasoning model is promising in addressing this deficiency.

## References

[Agarwal *et al.*, 2025] Sandhini Agarwal, Lama Ahmad, Jason Ai, Sam Altman, Andy Applebaum, Edwin Arbus, Rahul K Arora, Yu Bai, Bowen Baker, Haiming Bao, et al. gpt-oss-120b & gpt-oss-20b model card. *arXiv preprint arXiv:2508.10925*, 2025.

[Akyürek *et al.*, 2024] Ekin Akyürek, Mehul Damani, Adam Zweiger, Linlu Qiu, Han Guo, Jyothish Pari, Yoon Kim, and Jacob Andreas. The surprising effectiveness of test-time training for few-shot learning. *arXiv preprint arXiv:2411.07279*, 2024.

[Başar *et al.*, 2001] Erol Başar, Canan Başar-Eroglu, Sirel Karakaş, and Martin Schürmann. Gamma, alpha, delta, and theta oscillations govern cognitive processes. *International journal of psychophysiology*, 39(2-3):241–248, 2001.

[Brown *et al.*, 2020] Tom Brown, Benjamin Mann, Nick Ryder, Melanie Subbiah, Jared D Kaplan, Prafulla Dhariwal, Arvind Neelakantan, Pranav Shyam, Girish Sastry, Amanda Askell, et al. Language models are few-shot learners. *Advances in neural information processing systems*, 33:1877–1901, 2020.

[Buzsáki, 2006] György Buzsáki. *Rhythms of the Brain*. Oxford university press, 2006.

[Chollet, 2019] François Chollet. On the measure of intelligence. *arXiv preprint arXiv:1911.01547*, 2019.

[Dosovitskiy, 2020] Alexey Dosovitskiy. An image is worth 16x16 words: Transformers for image recognition at scale. *arXiv preprint arXiv:2010.11929*, 2020.

[Foundation, 2026] ARC Prize Foundation. Arc-ag1 benchmarking: Leader-board and dataset for the arc-ag1 benchmark, 2026.

[Guo *et al.*, 2025] Daya Guo, Dejian Yang, Haowei Zhang, Junxiao Song, Ruoyu Zhang, Runxin Xu, Qihao Zhu, Shiron Ma, Peiyi Wang, Xiao Bi, et al. Deepseek-r1: Incentivizing reasoning capability in llms via reinforcement learning. *arXiv preprint arXiv:2501.12948*, 2025.

[Hodel, 2024] Michael Hodel. Addressing the abstraction and reasoning corpus via procedural example generation, 2024.

[Hu *et al.*, 2025] Keya Hu, Ali Cy, Linlu Qiu, Xiaoman De-lores Ding, Runqian Wang, Yeyin Eva Zhu, Jacob Andreas, and Kaiming He. ARC is a vision problem!, 2025.

[Huntenburg *et al.*, 2018] Julia M Huntenburg, Pierre-Louis Bazin, and Daniel S Margulies. Large-scale gradients in human cortical organization. *Trends in cognitive sciences*, 22(1):21–31, 2018.

[Jolicoeur-Martineau, 2025] Alexia Jolicoeur-Martineau. Less is more: Recursive reasoning with tiny networks, 2025.

[Lee *et al.*, 2015] Chen-Yu Lee, Saining Xie, Patrick Gallagher, Zhengyou Zhang, and Zhuowen Tu. Deeply-Supervised Nets. In Guy Lebanon and S. V. N. Vishwanathan, editors, *Proceedings of the Eighteenth International Conference on Artificial Intelligence and Statistics*, volume 38 of *Proceedings of Machine Learning Research*, pages 562–570, San Diego, California, USA, 09–12 May 2015. PMLR.

[LeGris *et al.*, 2024] Solim LeGris, Wai Keen Vong, Brenden M Lake, and Todd M Gureckis. H-arc: A robust estimate of human performance on the abstraction and reasoning corpus benchmark. *arXiv preprint arXiv:2409.01374*, 2024.

[Lin *et al.*, 2017] Tsung-Yi Lin, Priya Goyal, Ross Girshick, Kaiming He, and Piotr Dollár. Focal loss for dense object detection. In *Proceedings of the IEEE international conference on computer vision*, pages 2980–2988, 2017.

[Long *et al.*, 2015] Jonathan Long, Evan Shelhamer, and Trevor Darrell. Fully convolutional networks for semantic segmentation. In *Proceedings of the IEEE conference on computer vision and pattern recognition*, pages 3431–3440, 2015.

[Murray *et al.*, 2014] John D Murray, Alberto Bernacchia, David J Freedman, Ranulfo Romo, Jonathan D Wallis, Xinying Cai, Camillo Padoa-Schioppa, Tatiana Pasternak, Hyojung Seo, Daeyeol Lee, et al. A hierarchy of intrinsic timescales across primate cortex. *Nature neuroscience*, 17(12):1661–1663, 2014.

[Pahor and Jaušovec, 2014] Anja Pahor and Norbert Jaušovec. Theta–gamma cross-frequency coupling relates to the level of human intelligence. *Intelligence*, 46:283–290, 2014.

[Ronneberger *et al.*, 2015] Olaf Ronneberger, Philipp Fischer, and Thomas Brox. U-net: Convolutional networks for biomedical image segmentation. In *International Conference on Medical image computing and computer-assisted intervention*, pages 234–241. Springer, 2015.

[Sun *et al.*, 2020] Yu Sun, Xiaolong Wang, Zhuang Liu, John Miller, Alexei Efros, and Moritz Hardt. Test-time training with self-supervision for generalization under distribution shifts. In *International conference on machine learning*, pages 9229–9248. PMLR, 2020.

[Tort *et al.*, 2009] Adriano BL Tort, Robert W Komorowski, Joseph R Manns, Nancy J Kopell, and Howard Eichenbaum. Theta–gamma coupling increases during the learning of item–context associations. *Proceedings of the National Academy of Sciences*, 106(49):20942–20947, 2009.

[Vaswani *et al.*, 2017] Ashish Vaswani, Noam Shazeer, Niki Parmar, Jakob Uszkoreit, Llion Jones, Aidan N Gomez, Łukasz Kaiser, and Illia Polosukhin. Attention is all you need. *Advances in neural information processing systems*, 30, 2017.

[Wang *et al.*, 2025] Guan Wang, Jin Li, Yuhao Sun, Xing Chen, Changling Liu, Yue Wu, Meng Lu, Sen Song, and Yasin Abbasi Yadkori. Hierarchical reasoning model, 2025.

[Zeraati *et al.*, 2023] Roxana Zeraati, Yan-Liang Shi, Nicholas A Steinmetz, Marc A Gieselmann, Alexander Thiele, Tirin Moore, Anna Levina, and Tatiana A Engel. Intrinsic timescales in the visual cortex change with

selective attention and reflect spatial connectivity. *Nature communications*, 14(1):1858, 2023.